1991AJ....102..795D

THE ASTRONOMICAL JOURNAL VOLUME 102, NUMBER 2 AUGUST 1991

RADIO IMAGES OF JUPITER'S SYNCHROTRON RADIATION AT 6, 20, AND 90 cm

IMKE DE PATER
Astronomy Department, 601 Campbell Hall, University of California, Berkeley, California 94720

Received 17 January 1991; revised 3 May 1991

ABSTRACT

VLA observations of Jupiter's nonthermal radiation at wavelengths of 6, 20, and 90 cm are presented and compared. The spatial resolution in all images is 0.25 R_J (R_J = Jovian radius). The brightness distribution of Jupiter is very similar at each of the three wavelengths, although the radiation peaks at 6 cm are at a slightly larger distance from Jupiter than those at the longer wavelengths. This is due to the higher rate of synchrotron radiation losses at the shorter wavelengths. Radial profiles through the images clearly show the presence of a "shoulder" or flattening in the intensity at $\sim 2.5\ R_J$ due to absorption effects by the satellite Amalthea. In addition, the so-called "hot region" in Jupiter's radiation belts is clearly present at all three wavelengths: images of the planet at a cml (central meridian longitude) of $\sim 30°$–$40°$ show the radiation peak to the right of Jupiter to be much brighter than the peak at the left, while images at a cml of $\sim 210°$–$220°$ show the opposite. The difference in brightness between the two radiation peaks is similar at all three wavelengths. Measurements of the total intensity confirm earlier results which showed a flattening of the radio spectrum at longer wavelengths, or a decrease in spectral index with increasing wavelength: $\alpha = 0.35 \pm 0.05$ between 6 and 20 cm, and $\alpha = 0.13 \pm 0.04$ between 20 and 90 cm.

1. INTRODUCTION

Jupiter's synchrotron radiation was first detected in the late fifties, and has been observed regularly since that time (see review papers by, e.g., Berge & Gulkis 1976; Carr *et al.* 1983; de Pater & Klein 1989; de Pater 1990). The strength and shape of the planet's magnetic field was largely derived from these and longer wavelength (decametric) observations about a decade before the first spacecraft (Pioneer 10) encounter. Although this and subsequent spacecraft encounters provided a wealth of information on Jupiter's magnetosphere, the inner few Jovian radii remained little explored. Only Pioneer 11 approached the planet to a distance less than 3 R_J (1R_J is 1 Jovian radius), and that along a fast north–south trajectory. Hence, the inner few Jovian radii are still best explored through ground-based observations of the decimetric and decametric emissions from the planet.

Synchrotron radiation is emitted by relativistic electrons gyrating around magnetic field lines. The radiation is beamed in the forward direction within a cone $1/\gamma$, with $\gamma = 2E$, and E the energy of the radiating electron in MeV. The radiation is emitted over a wide range of frequencies, but shows a maximum at $0.29\nu_c$, with ν_c the critical frequency (in MHz),

$$\nu_c = 16.08E^2B, \tag{1}$$

and B the magnetic field strength in units of Gauss. Thus for a constant B the peak emission at different observing frequencies is emitted by electrons with different energies. The typical energy of electrons radiating at 20 cm, with $B = 0.5$ G is close to 25 MeV, while electrons radiating at 6 cm require energies of ~ 45 MeV, and at 90 cm of ~ 12 MeV. If the spatial distribution of the electrons would be independent of energy, then the radio images at different wavelengths should be identical. Of course, the relative strengths of the flux densities would depend upon the spectrum of the radiating particles.

Based upon the similarity of beaming curves of Jupiter's radio emission (the variation of Jupiter's emission with the planet's rotation) at wavelengths between 6 and 50 cm, Roberts & Komesaroff (1968) suggested that the spatial distribution of the relativistic electrons is independent of energy. Beaming curves at longer wavelengths, however, showed much less variation with Jovian longitude.

De Pater (1980) showed that the spatial extent of Jupiter's synchrotron emission is equal at wavelengths between 6 and 50 cm. Branson (1968) observed at both 20 and 75 cm wavelength, and noticed that the emission region at 75 cm was slightly larger than that at 20 cm. This would suggest an enhancement of low energy particles at larger distances from Jupiter, or a softening of the electron spectrum with increasing distance to the planet. A similar conclusion was reached by de Pater (1981b) and de Pater & Goertz (1990), who simulated Jupiter's synchrotron radiation using radial diffusion models for the energetic electrons. The latter investigations suggested that Jupiter's microwave spectrum required an electron spectrum which was harder than that observed at Io's orbit by the various spacecraft.

To investigate this possible discrepancy in the spatial distribution of low and high energetic electrons, Jupiter was imaged at wavelengths of 6, 20, and 90 cm to intercompare the detailed shape of the emission region at these wavelengths.

2. OBSERVATIONS AND DATA REDUCTION

All observations of Jupiter reported in this paper were carried out with the VLA (Very Large Array)[1] at 6, 20, and 90 cm wavelength (4885, 1465, and 333 MHz). The bandwidth used for the observations was 50 MHz at 6 and 20 cm, and 3 MHz at 90 cm. To facilitate comparison of radio images at different frequencies, the object should be observed with the same angular resolution. We, therefore, imaged Jupiter with different array configurations. The 6, 20, and 90 cm data were obtained in the C, B, and A array, respectively. Details of the observations are summarized in Table 1: the observing wavelength, array configuration, UT date, secondary calibrator source, approximate right ascension and declination of Jupiter, Geocentric distance, apparent size and position angle of the rotation axis of the planet, the decli-

---

[1] The VLA is a facility of the National Radio Astronomy Observatory, which is operated by Associated Universities, Inc., under contract with the National Science Foundation.

0004-6256/91/020795-11$00.90

1991AJ....102..795D

nation of the Earth, and the resolution in arcsec. The beamsize for the final images was chosen such that the resolution of the radio images in each configuration was equal to 0.25 R_J.

TABLE 1. VLA observations of Jupiter.

Wavelength (cm)	Array configuration	Date (UT)	Calibration source	R.A.	Dec.	Geocentric distance (AU)	Apparent size equ	Apparent size pole	P.A.	Declination Earth	Restoring beam
6.14	B	1982 Jul 23/24	1334-127	13h 58m	− 10°55′	5.30	37.1″	34.7″	21°5	− 2°88	4.64″
6.14	C	1983 Apr 15/16	1730-130	16h 35m	− 21°05′	4.62	42.7″	39.9″	8°1	− 3°08	5.34″
21.2	B	1982 Jul 23/24	1349-145	13h 58m	− 10°55′	5.30	37.1″	34.7″	21°5	− 2°88	4.64″
20.5	B	1987 Dec 13/14	0056-001	01h 15m	+ 06°27′	4.41	44.7″	41.8″	− 23°8	+ 3°28	5.59″
20.5	B	1989 Apr 22/23	0428 + 205	04h 24m	+ 21°06′	5.97	33.7″	31.5″	− 9°2	+ 3°10	4.20″
90.1	B	1987 Dec 13/14	3C48	01h 15m	+ 06°27′	4.41	44.7″	41.8″	− 23°8	+ 3°28	(Total flux only)
90.1	A	1988 Dec 20/21	3C138	03h 43m	+ 18°44′	4.17	47.3″	44.2″	− 13°4	+ 3°58	5.91″
90.1	B	1989 Apr 22/23	3C138	04h 24m	+ 21°06′	5.97	33.7″	31.5″	− 9°2	+ 3°10	(Total flux only)

In order to measure Jupiter's total flux density at any of these wavelengths, data should be obtained with a single dish or a very compact array configuration. Since our primary purpose was to obtain high resolution images, no accurate information on the total flux densities could be obtained at 6 and 20 cm, due to the lack of short spacing data. However, a reasonably accurate estimate of the total flux density at 90 cm could be obtained, since the planet was also observed at this wavelength in a more compact array configuration, simultaneously with the 20 cm observations.

The gain of the antennas was calibrated on 3C286 before 1987, and on 3C48 afterwards. We assumed flux densities from the scale of Baars *et al.* (1977), adjusted for variability at 6 cm for 3C48 found from monitoring its flux density by the VLA staff. Phase calibration was performed on the sources listed in Table 1, column 4. Internal uncertainties in the flux density calibration are believed not to exceed 3%; absolute calibration is likely accurate to $\lesssim 5\%$ (Baars *et al.* 1977). After the spatial frequency data were edited and calibrated, they were gridded and Fourier transformed to give maps of Jupiter's brightness distribution. Images of the planet were obtained at different longitudes, each integrated over approximately 25 min, which gives a smearing in the images equal to $\sim 15\%$ of Jupiter's rotation. This corresponds to a smearing of $\sim 0.25 R_J$ at the subsolar point. The images of the total flux density at 6 and 20 cm were deconvolved using a CLEAN method, specially adapted to observations of planets (e.g., de Pater & Dickel 1986; de Pater 1990). The image of the total flux density at 90 cm, as well as the images of the polarized flux density (Stokes parameters Q and U) were deconvolved using the conventional CLEAN algorithm (Högbom 1974; Clark 1980).

The sequence of images obtained in this way shows Jupiter's brightness distribution over a complete set of rotational aspects. Such a data cube is a prerequisite for the development of a three-dimensional magnetospheric model. An accurate comparison of the brightness distribution of Jupiter's radio emission at all three wavelengths would require images with a high signal-to-noise ratio at each of the wavelengths. Such images can be obtained after integrating on the source for many hours. Unfortunately, for Jupiter this would result in a smearing of the brightness distribution, due to wobbling of Jupiter's magnetic field axis, which is inclined by $\sim 10°$ with respect to its rotation axis (Morris & Berge 1962). This can best be seen from the sequence of images obtained during one Jovian rotation (e.g., de Pater 1980; de Pater & Jaffe 1984). To circumvent this smearing problem in the observations, the spatial frequency or *uv* data at each longitude bin of 15° were rotated such that the peak emissions from the radiation belt were aligned along the R.A. direction. The data from all longitude bins were then combined, and images of the total intensity were constructed. This method of averaging the *uv* data cannot be used to create a high signal-to-noise image of Jupiter's polarized emission, due to the directional nature of the Q and U images. Such an image was constructed by combining the images, rather than the *uv* data of the polarized flux density at each rotational aspect, after proper rotation. Note that the images obtained after combining all the data can only be used to compare the general brightness distribution at each wavelength. For investigation of east–west asymmetries in the images, one needs to use the individual images at each longitude bin.

In addition to the improvement in signal-to-noise ratio, the rotation and summation of the *uv* data decreased the background confusion considerably, as was in particular noticeable in the 90 cm images.

The thermal emission from Jupiter at 6 cm from the dataset presented here has already been discussed by de Pater & Dickel (1986). It should be noted that, because of the misalignment between the magnetic and true rotation axes, different data reduction methods are needed for studies of the nonthermal (magnetic axis related) and thermal (rotational axis related) emission from Jupiter. In the present paper the data at each rotational aspect, integrated over 15° of Jovian longitude, were rotated such that the radiation belts coincide; hence the thermal emission is smeared out, and no latitudinal variations on the disk can be distinguished.

The 20 cm data were taken as part of the Jupiter Patrol program at the VLA, where, since 1981, the planet is observed approximately every 15 months in the B configuration. When data have been obtained over a full Jovian year (12 Earth years), a detailed analysis of the entire sequence of images will be presented.

3. RESULTS

3.1 Total Flux Density

Jupiter's total flux density is best determined from observations with single element radio telescopes, or using model fits to *uv* data obtained in compact array configurations. Since the Fourier transform of a double point source is a cosine function, and that of a single or double square signal a sinc function, we expect Jupiter's visibility data at short spacings to behave more or less like a cosine function. We, therefore, estimated the planet's total flux density by fitting a cosine function through the short spacing visibility data. The results are shown in Figs. 1(a)–1(d). The average total flux

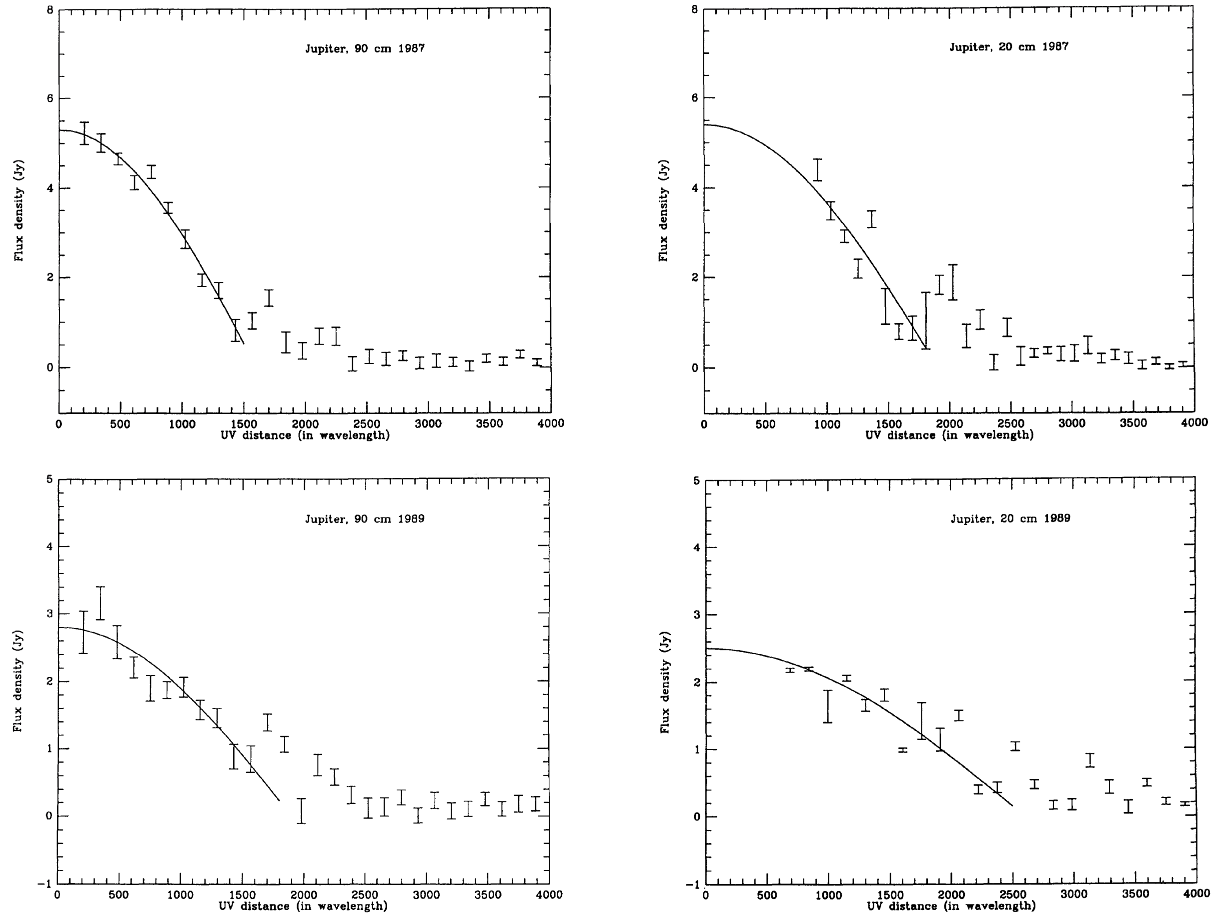

FIG. 1. Plots of the real part of the visibility data (in Jy) as a function of *uv* distance (in wavelengths), for the 90 and 20 cm data from 1987 and 1989. The best fit is superimposed on the data.

density at 90 cm is 5.3 ± 0.12 Jy in 1987, and 2.8 ± 0.14 Jy in 1989. After subtraction of Jupiter's thermal contribution, and adjusting the flux density of the planet to its standardized distance of 4.04 AU, the total nonthermal flux densities are 6.32 ± 0.14 Jy in 1987, and 6.03 ± 0.30 Jy in 1989 (at 4.04 AU the thermal flux density is ~0.08 Jy). Averaged flux densities at 20 cm are less accurate, since practically no data were obtained at short interferometer spacings [see Figs. 1(c) and 1(d)]. To determine Jupiter's spectrum, however, we need to determine the total nonthermal flux densities from data at two wavelengths taken nearly simultaneously in time, because the planet's flux density is known to vary (e.g., Klein *et al.* 1989). After correcting the total measured flux densities to the standardized distance of 4.04 AU, and after subtraction of the thermal flux density ~0.9 Jy at 4.04 AU, the total nonthermal flux densities at 20 cm are 5.53 ± 0.35 Jy in 1987, and 4.65 ± 0.39 Jy in 1989.

To investigate Jupiter's beaming curve at 90 cm, the planet's total flux density was also determined at the individual Jovian longitudes, using the same modeling procedure as mentioned above. Unfortunately, the uncertainty in these small datasets is rather large. Nevertheless, in 1987 one can distinguish a sinusoidal variation in the graph of the planet's flux density versus Jovian longitude. This beaming curve is shown in Fig. 2. In 1989, when the planet was at a larger distance from Earth, the *uv* data are too noisy to determine the flux density from the system at individual longitudes. Superimposed on Fig. 2 is a beaming curve as expected for 13–20 cm observations at the December 1987 epoch

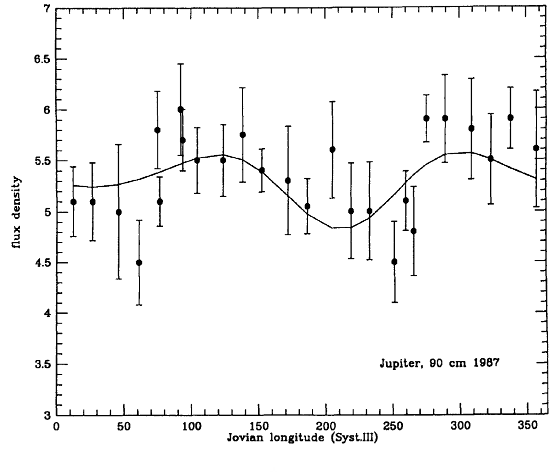

FIG. 2. The beaming curve of Jupiter at 90 cm, from 1987. Superimposed is the beaming curve expected for this epoch in time.

($D_E = +3.28°$) (Klein *et al.* 1989). We conclude from this that Jupiter's beaming curve at 90 cm is rather similar to that at shorter wavelengths.

3.2 Shape of the Radiation Belts at 6, 20, and 90 cm Wavelengths

The final images of Jupiter's total flux and linearly polarized intensity at 6, 20, and 90 cm are shown in Figs. 3(a)–3(f). The images are displayed such that the scale expressed in Jovian radii is the same for each map. The images of both the total and linearly polarized flux are remarkably similar at the different wavelengths: the overall shape and linear extent of the nonthermal emission region and the position of the radiation peaks are the same at all wavelengths. In the images of the total intensity one can see the increase in the thermal contribution with decreasing wavelength. Note that the thermal emission at 90 cm is below the detection limit of the telescope; the total thermal flux density expected at this wavelength is ~0.07 Jy. In addition to the fact that the position of the radiation peaks at the different wavelengths is equal, the positions of the peak intensities in the total and linearly polarized flux density images are also the same.

To better illustrate the similarities between the various images, east–west cuts along the equator through the images of the total intensity and linearly polarized flux density are displayed in Figs. 4(a) and 4(b), respectively. The scans at the three wavelengths are superimposed: light dotted lines at 6 cm, solid lines at 20 cm, and dashed lines at 90 cm. The flux densities were normalized to the peak flux density at 20 cm. As mentioned above, the position of the radiation peaks at all wavelengths coincide, and the shape of the scans are very similar. Obviously, the thermal flux density from the planet [Fig. 4(a)] increases from less than about one mJy/beam at 90 cm to ~180 mJy/beam at 6 cm (at 4.04 AU). Note that most of the radiation from Jupiter's "disk" at 90 cm is of nonthermal origin, as can be judged from the scans through the polarized images.

3.3 Longitudinal Dependence of the Emission

As first noticed by Branson (1968), and later by de Pater & Dames (1979), there is a pronounced asymmetry in intensity between the two radiation peaks, located on either side of Jupiter, at any given cml (central meridian or sub-Earth longitude). At a cml of ~180°–260°, the peak at the east side of the planet is brighter than that at the west side, while the reverse is true at a cml of ~0°–60°. This was interpreted to be due to a "hot spot" in the radiation belts, at a particular longitude, thus rotating with the planet. Branson's (1968) images suggested the "hot spot" to be at a longitude of ~200°, but later data (de Pater & Dames 1979; de Pater 1980; de Pater & Jaffe 1984) showed this region at a longitude of 250°–260°. To examine the behavior of the asymmetry during a Jovian rotation, and thus location of this "hot spot," Fig. 5 shows graphs of the difference between the peak intensities of the two radiation belts ($I_{\text{left}} - I_{\text{right}}$) as a function of Jovian longitude (System III, 1965.0). The flux density of the radiation peaks changes with Jupiter's geocentric distance, r_g, due to a combined effect of the increase/decrease in intensity according to the r_g^2 law, and the fact that the missing short spacing problem gets more severe with decreasing geocentric distance. The peak intensity in every sequence of images, which usually is near a longitude of 100° or 300°, at each wavelength and polarization was therefore scaled to 150 mJy/beam. Since the shape of the resulting curves $I_{\text{left}} - I_{\text{right}}$ also depends upon the viewing geometry of the planet, one can expect pronounced changes with D_E, the declination of the Earth. To investigate possible variations in the longitudinal behavior between different wavelengths, graphs of the difference in intensity between the two radiation peaks were made from each of the series of images at the three wavelengths, and compared with curves at 20 cm, at roughly the same D_E and geocentric distance. The first row in Fig. 5 shows the longitudinal behavior of the difference in intensity between the radiation peaks in the images of the total intensity at 20 and 90 cm. The second row shows the behavior in the polarized images at these wavelengths, and the third row shows the behavior in polarized images at 20 and 6 cm wavelength. The observations for the 20/90 cm comparison (rows 1 and 2) were obtained when D_E was positive, between 3.1° and 3.6°, while the data for the 20/6 cm comparison were obtained at negative D_E, $D_E \sim -3°$. The date of the observations and D_E is indicated at the top of each graph.

4. DISCUSSION

4.1 Spectrum

The shape of Jupiter's spectrum between 6 and 50 cm wavelength has been addressed in the past by, e.g., Neidhöfer *et al.* (1977), de Pater & Dames (1979), and de Pater & Goertz (1990; hereafter referred to as dPG). Since the total flux density of the planet is known to change with time (e.g., Klein *et al.* 1989), an accurate spectrum of Jupiter's synchrotron radiation can only be obtained if the planet is observed simultaneously at different wavelengths. Since short spacing data are a must to determine the total flux density, the measurements should be made with single dish radio telescopes or compact array configurations. In addition, Jupiter's spectrum may also change in time, as became evident in 1973 when Jupiter's nonthermal flux density decreased by ~35% at 21 cm, but only by ~25% at 11–13 cm (Klein 1976). This would change the spectral index considerably.

Table 2 shows a summary of the spectral indices for Jupiter's nonthermal emission obtained between different wavelengths. This spectral index α is defined such that $S_\nu = \text{Const} \times \nu^{-\alpha}$, with S_ν the flux density at frequency ν. From the theory of synchrotron radiation one can relate the radio spectral index, α, to the electron spectrum $N(E)dE \sim E^{-\gamma}dE$, via $\gamma = 1.0 + 2\alpha$. The latter numbers are also shown in Table 2. Despite possible time variations in Jupiter's spectrum, the numbers strongly suggest that Jupiter's radio spectrum becomes flatter with increasing wavelength. This confirms results obtained before by, e.g., Neidhöfer (1978), and de Pater & Dames (1979). It is also consistent with the general shape of electron spectra measured by spacecraft flybys (see Van Allen 1976). It should be noted, however, that the electron spectra obtained from the radio data are typically harder than the Pioneer spectra, as shown by, e.g., dPG. The latter authors calculated the radio spectral index expected from electrons diffusing inwards from $L = 6$, having an energy dependence at $L = 6$ as measured by the Pioneer spacecraft. They obtained a spectral index $\alpha \sim 0.50 - 0.55$ for the entire wavelength range, which is much larger than the measured ground-based values. dPG attributed this to energy degradation of energetic electrons caused by the dust particles in Jupiter's ring. After inclusion

1991AJ....102..795D

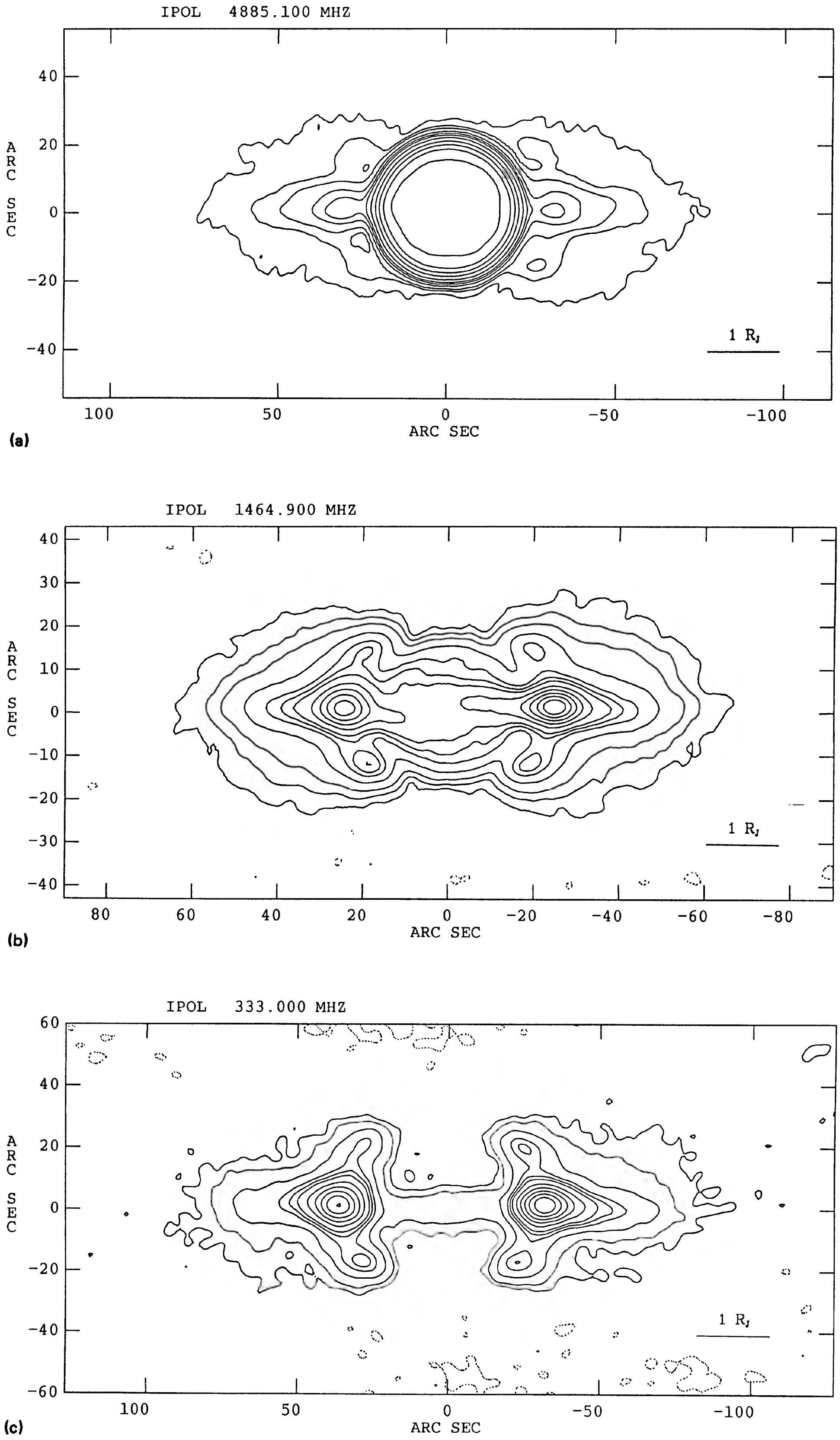

FIG. 3. Images of Jupiter's brightness distribution at 6, 21, and 90 cm. Images of both the total intensity [(a)–(c)] and linearly polarized flux density [(d)–(f)] are shown. All images are averaged over all rotational aspects (see text). The FWHP beam width is 0.25R_J in all images (see Table 1 for conversion to arcsec). Contour values are (in % of peak flux density): (a) 6 cm: 1%, 3%, 5%, 10%, 15%, 20%, 30%, 45%, 60%, 75%, 90% of the peak flux density of 147 mJy-/beam. (b) 20 cm: 2%, 5%, 10%, 20%, 30%, 35%, 40%, 50%, 60%, 70%, 80%, 90% of the peak flux density of 36.5 mJy/beam. (c) 90 cm: 5%, 10%, 20%, 30%, 35%, 40%, 50%, 60%, 70%, 80%, 90% of the peak flux density of 66.5 mJy/beam. (d)–(f) 10%, 20%, 25%, 30%, 40%, 50%, 60%, 70%, 80%, 90% of the peak flux density. The peak flux density is 19.4 mJy/beam at 6 cm, 21.3 mJy/beam at 20 cm, and 35.7 mJy/beam at 90 cm.

1991AJ....102..795D

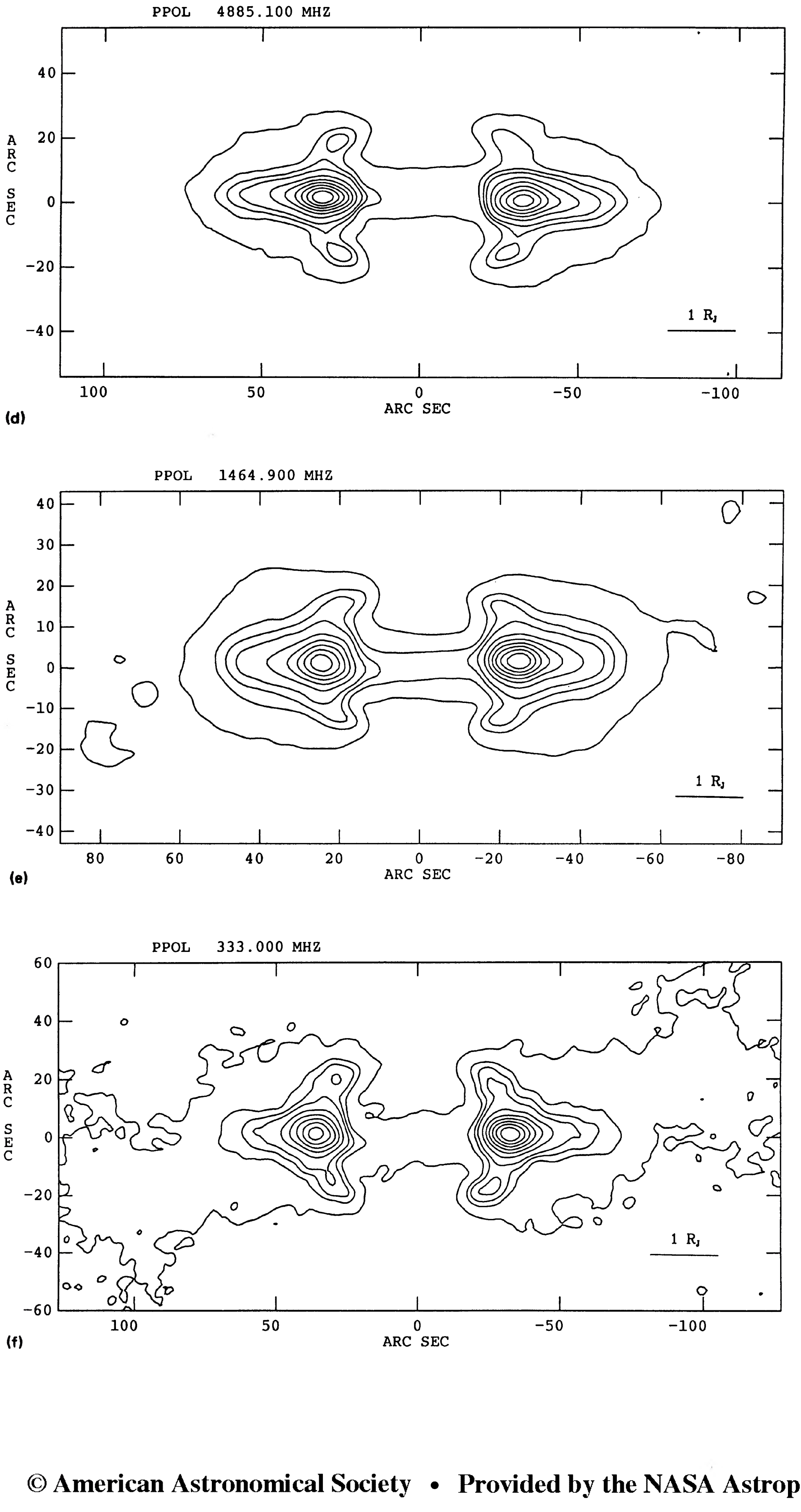

FIG. 3 (continued)

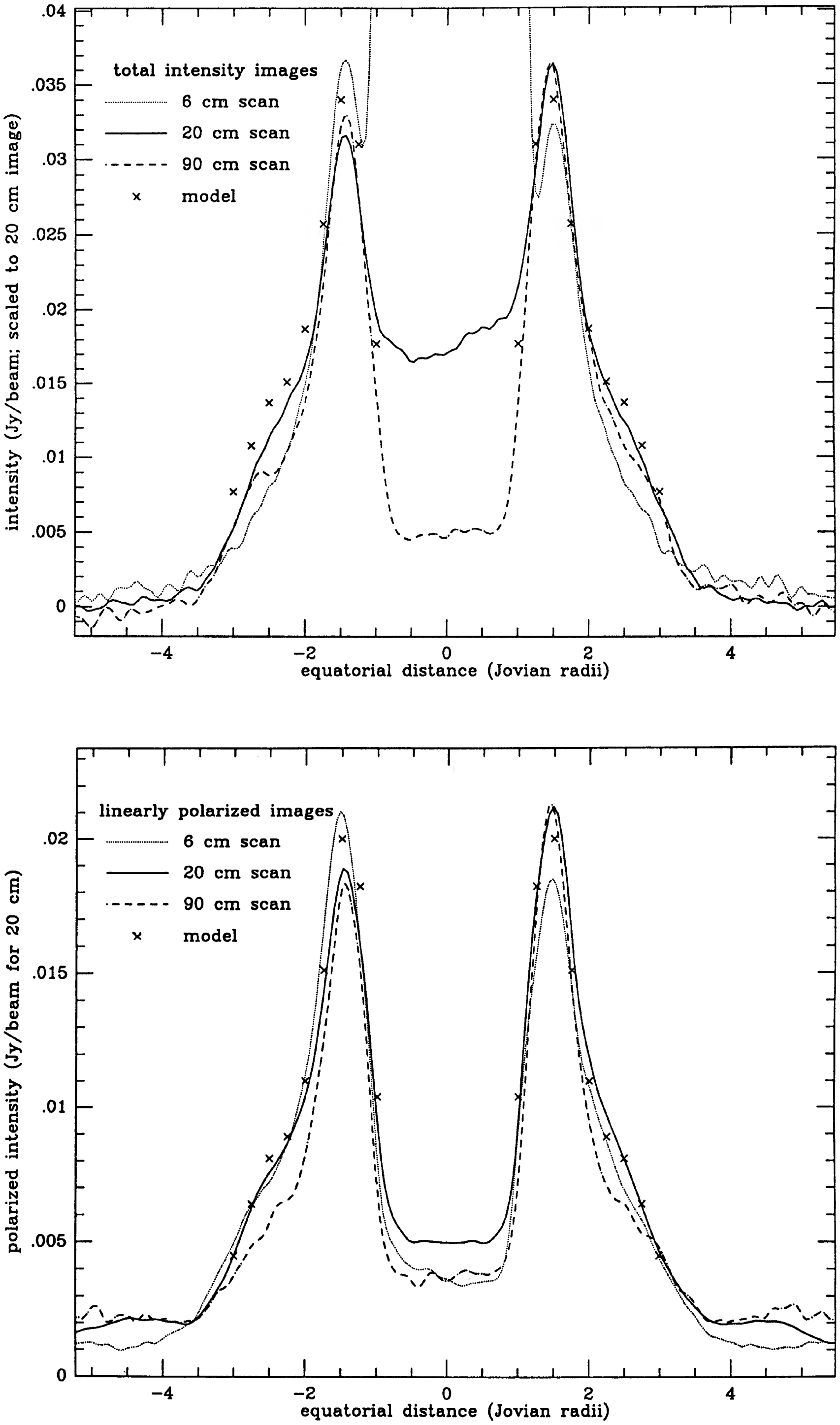

FIG. 4. Radial profiles through the total intensity and linearly polarized flux density images from Fig. 3. The crosses on the figures outline the profile from de Pater's (1981b) model calculations.

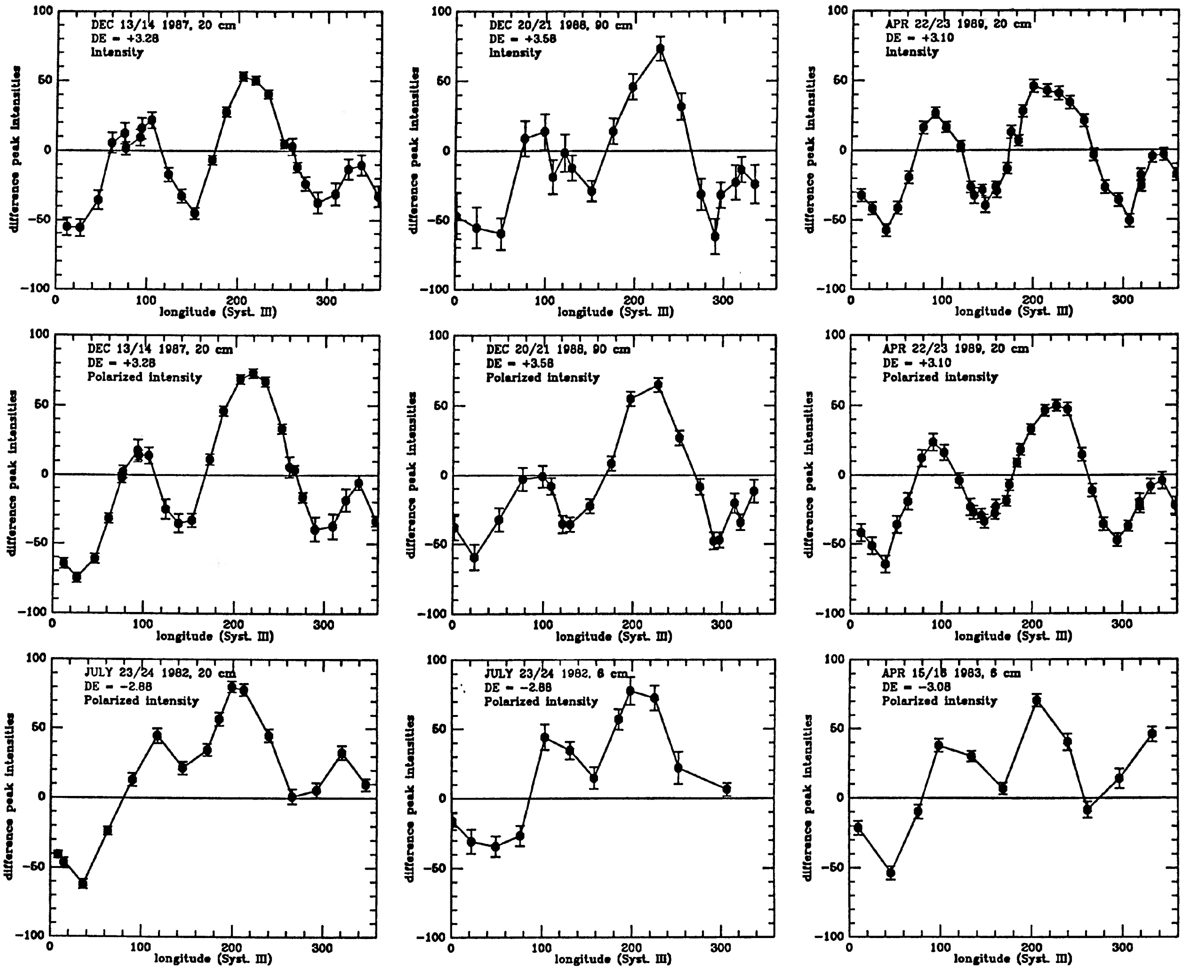

FIG. 5. Graphs of the difference in peak intensity $I_{\rm left} - I_{\rm right}$ (in mJy/beam) as a function of Jovian longitude. The peak intensity in every data set was scaled to 150 mJy/beam. The top row shows the results for the total intensity at 20 and 90 cm when $D_E \sim 3.1$–$3.6°$; the second row shows the graphs for polarized flux density, and the bottom row for the polarized flux density at 6 and 20 cm, when $D_E \sim -3°$.

of this effect in their calculations they obtained a radio spectral index $\alpha = 0.20$ ($\gamma = 1.40$) between 20 and 90 cm, and $\alpha = 0.34$ ($\gamma = 1.68$) between 6 and 20 cm, which is much closer to the values determined in this paper.

4.2 Spatial Brightness Distribution

As shown in Fig. 3, the spatial brightness distribution of Jupiter's synchrotron emission is very similar at all three wavelengths, both in total and linearly polarized flux density. The extent of the emitting region is $3.5R_J$, and the radio emission is confined to the magnetic equator up to $\sim 3R_J$. The secondary emission peaks north and south of the main peaks are also present at all wavelengths. The radiation is likely confined to the magnetic equator due to absorption effects from Thebe at $3.1R_J$ (de Pater 1983). The secondary emission peaks are caused by electrons at their mirror points. These are electrons with small pitch angles (angle between the magnetic field direction and the particle's motion),

TABLE 2. Spectral index for Jupiter's nonthermal emission.

Wavelengths	Spectral index α	γ	Year	Reference
6–21 cm	0.37 ± 0.08	1.74 ± 0.16	1977–1978	de Pater 1981b; updated by dPG
11–21 cm	0.34 ± 0.07	1.68 ± 0.14	1963–1976	Neidhöfer *et al.*, 1977
	0.35	1.70	1963–1970	
	0.29	1.58	1974–1976	
21–50 cm	0.11 ± 0.07	1.22 ± 0.14	1973	de Pater & Dames 1979; updated by dPG
21–90 cm	0.09 ± 0.045	1.18 ± 0.09	1987	this paper
21–90 cm	0.19 ± 0.07	1.38 ± 0.14	1989	this paper

1991AJ....102..795D

which cross the magnetic equator between 2 and $3R_J$ (de Pater 1983).

As displayed in Fig. 4, the radiation peaks seem to be superimposed on a broader emission component. The presence of the "shoulders" in the emission profile was first noted by de Pater (1981a), and are thought to be due to absorption effects by Amalthea, at $2.5R_J$ from the planet. In Fig. 4(a) the 6 cm scan drops off faster with increasing planetary distance than the scans through the 20 and 90 cm images. However, the 6 cm radiation peak is only a fraction, ~15%, of the thermal radiation, so the outer parts of the radiation belts at 6 cm are likely less reliable. The 6 cm scan through the polarized emission is more similar to the 20 cm scan. On the other hand, the scan through the polarized emission at 90 cm seems to drop off faster than those at the two other wavelengths.

The location of the radiation peaks (1.45–$1.48R_J$) coincides within $0.03R_J$ at the different wavelengths, despite the fact that the data were all taken at different times. We have to be cautious here, since it is known that the location of the radiation peaks varies with time. In a review paper by de Pater & Klein (1989) it is shown that the distance between the radiation peaks decreased from $1.6R_J$ in the late Sixties to $\sim 1.3R_J$ in the early Seventies, after which it increased again. We show de Pater and Klein's graph in Fig. 6, updated with data obtained with the VLA Jupiter Patrol program (see Sec. 2). The figure shows the distance between the radiation peaks, expressed in Jovian radii, as a function of time. The 11–20 cm data show a clear long-term variation in the distance between the radiation peaks; short-term time variability might be present as well. It is interesting to compare the distance between the radiation peaks at wavelengths longer and shorter than the 11–20 cm wavelength range. One can see that the values at longer wavelengths (90 cm) are rather similar to those taken at 20 cm at about the same time. Data at shorter wavelengths (3.7–6 cm), however, usually show a somewhat larger value than the nearby 11–20 cm points. Hence, the fact that the position of the radiation peaks is so similar in the three images presented in this paper is misleading. We happened to have observed Jupiter at 6 cm wavelength at a time (1983) when the 20 cm radiation peaks were relatively close together, while the longer wavelength data were taken later (1987–1989), after the peaks had moved farther away from each other.

The new data continue to support the conclusion that the distance of the radiation peaks increases slightly with decreasing wavelength. This is likely due to the fact that the short wavelength emission is produced by more energetic electrons than the longer wavelength emission. It was shown in the Introduction [Eq. (1)] that the typical energy of electrons emitting at 20 cm is ~25 MeV, and those emitting at 6 cm is ~50 MeV, if the magnetic field strength is 0.5 G. The lifetime of electrons against synchrotron radiation losses, τ_s (in days), is approximately (de Pater 1981b):

$$\tau_s \sim 3.04\times 10^3/B^2E. \qquad (2)$$

At a Jovian distance of $1.4R_J$ the fieldstrength is ~1.6 G, which implies a typical energy of ~14 MeV for electrons radiating at 20 cm, and of ~26 MeV at 6 cm. The lifetimes of such electrons are 90 and 50 days, respectively. Since this is comparable to the timescales of inward radial diffusion (e.g., de Pater 1981b), the radio emission from electrons inside $\lesssim 1.4R_J$ decreases. Obviously, the higher energy electrons lose energy in a shorter time than lower energy particles, which explains the outward radial shift in the radiation peaks with decreasing observing wavelength. This observation is in agreement with model calculations by dPG.

The radiation profile, inclusive the "shoulders," was modeled by de Pater (1981b), and was shown to depend upon the survival probability of particles diffusing inward past Amalthea's orbit, and the amount of pitch angle scattering just inside the satellite's orbit. Since electrons with pitch an-

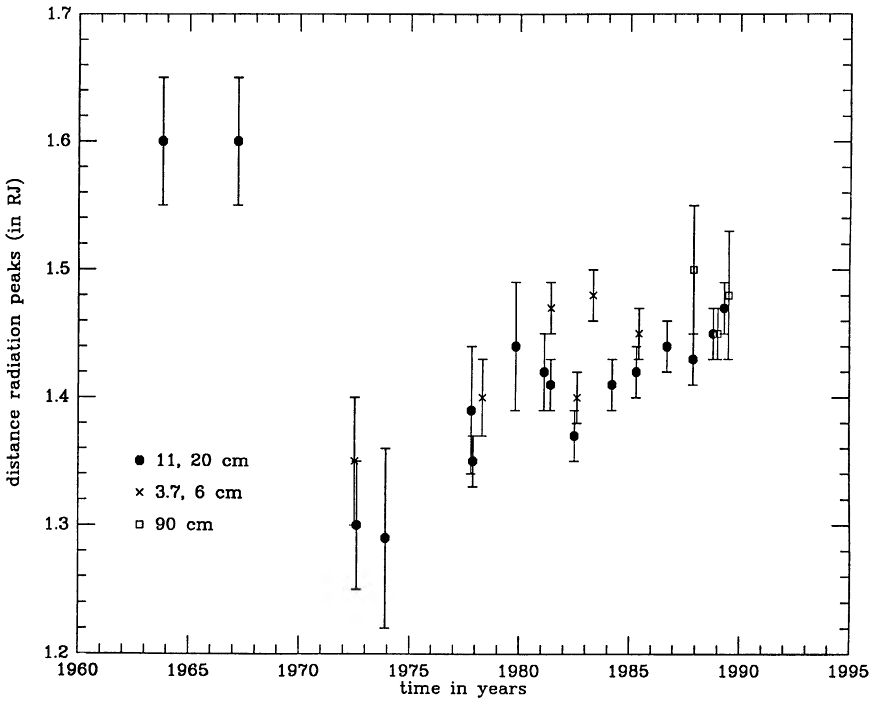

FIG. 6. The variation in radial distance of the peak intensities as a function of time (from de Pater & Klein 1989; updated with VLA Jupiter Patrol data).

gles ≲ 70° cross Jupiter's rotational equator twice during every bounce period, the chance of absorption by the satellites/rings is largest for the small pitch angle electrons. One of de Pater's (1981b) models [dashed line in her Fig. 14(d)] is superimposed as crosses on the radial scans displayed in Fig. 4. In this model calculation the survival probability of 20 MeV electrons was assumed to be 0.5, and she included a moderate amount of pitch angle scattering in the calculations. The agreement between this model and the new data is excellent. If the discrepancy between the radiation profiles at 20 and 90 cm is real, the absorption effects due to Jupiter's satellites are not independent of energy.

A detailed comparison of the present data with the radial profiles published by dPG show several discrepancies. The radiation peaks in dPG's calculations are closer to the planet and are steeper at the inside, dPG's profiles do not show the "shoulder" at $\sim 2.5R_J$, and are wider than the observed profile (above the "shoulder"), and furthermore the widths increase with decreasing wavelength. All these discrepancies can be explained by the fact that dPG's calculations were carried out for equatorially confined electrons in a pure dipole field, with the magnetic axis perpendicular to the line of sight. The images analyzed in this paper were obtained by combining the data in all longitude bins; thus the images are effectively integrated over all rotational aspects, and electrons over a wide range of pitch angles are sampled. Because the magnetic and rotational axes make a ~10° angle with each other and we receive emission from electrons which move practically along the line sight, the pitch angles of the electrons from which we receive emission depend upon Jupiter's orientation in the sky, thus the planet's central meridian longitude. Electrons which are confined to the magnetic equator (pitch angle 90°) can generally diffuse inward past the satellites without being absorbed. Particles with smaller pitch angles have a larger chance of being absorbed by one of the satellites or Jupiter's ring, because they bounce along the field lines between their mirror points, and often cross the orbital plane of the satellites (see, e.g., de Pater 1981b). Absorption of small pitch angle electrons by Amalthea cause the "shoulder" in the observed synchrotron radiation profile. Since such electrons were not included in dPG's calculations, they did not see this absorption effect in their calculations. In addition, the satellite absorption effects force the width of the radiation belts to be equal at all wavelengths.

Particles which bounce along the magnetic field lines usually spend most of the time at their mirror points. Since the magnetic field strength at these positions is much larger than that encountered in the magnetic equator on the same magnetic field line (or L shell), the lifetimes of these electrons is less than that of a 90° pitch angle electron. This will cause an outward shift of the peak intensity of the emission with respect to dPG's profile, and it will cause a more gradual decrease in intensity at the inside of the radiation peak, as observed.

4.3 Longitudinal Variation of the Emission

The longitudinal behavior of the emission characteristics, as displayed in Fig. 5, is also remarkably similar at the three wavelengths. The largest difference between the two peak intensities occurs at longitudes 210°–220° and 30°–40° at all three wavelengths. In the early years the peaks show up closer to 40° and 210°, while the later datasets show the peaks closer to 30° and 220°. In addition, note that also the general shape of the curves is somewhat different for the two different time epochs. We think that these discrepancies are due to the changing viewing geometry of the planet, and not to time variability. A detailed comparison of such curves at different D_E will be made in a few years, when VLA data have been obtained for a full Jovian year. These curves contain much information on both the magnetic field topology and the spatial distribution of the energetic electrons.

The difference in intensity between the two radiation peaks was originally interpreted to be due to a "hot spot" in the radiation belts. The existence of this "hot spot" is likely due to the combined effect of higher order terms in Jupiter's multipole magnetic field configuration and the presence of a dusk-to-dawn electric field over the inner magnetosphere (de Pater 1981c).

5. CONCLUSIONS

VLA observations of the brightness distribution of Jupiter's synchrotron radiation at 6, 20, and 90 cm are presented and compared. The spatial resolution of each image is equal to 0.25 Jovian radii. At 20 and 90 cm we are able to estimate the total nonthermal flux density from the planet, and determine the spectral index. A comparison of these values with numbers obtained previously by others shows that the spectral index decreases with increasing wavelength. On the average, the spectral index shortward of 20 cm is approximately $\alpha = 0.35 \pm 0.05$, and longward of 20 cm $\alpha = 0.13 \pm 0.04$. These values are consistent with the numbers obtained from inward radial diffusion models, only if energy degradation of energetic electrons by dust particles in Jupiter's ring is taken into account (de Pater & Goertz 1990).

The brightness distribution of Jupiter's synchrotron radiation is very similar at the three wavelengths. The extent of the emitting region is $\sim 3.5R_J$, and most of the emission is confined to the magnetic equatorial plane, due to absorption effects by Thebe, Amalthea, and Jupiter's ring. North and south of the main radiation peaks are secondary emission regions visible in all images, due to radiation from small pitch angle electrons at their mirror points. At $\sim 2.5R_J$ one can clearly distinguish a "shoulder" or flattening in intensity in the radial profiles, caused by Amalthea's absorption effects. The so-called "hot region" in Jupiter's radiation belts is seen at all three wavelengths: images of the planet at a central meridian longitude of ~30°–40° show the radiation peak to the right of Jupiter to be much brighter than the peak at the left, while images at ~210°–220° show the opposite. The existence of this "hot region" is likely due to the multipole character of the planet's magnetic field, in combination with a dusk-to-dawn electric field. The radial distance of the peak intensities is $\sim 1.46R_J$; the distance is slightly larger at 6 cm than at 20–90 cm, due to the fact that the electron energy, and thus synchrotron losses increase with decreasing wavelength. The radial profiles agree quite well with de Pater's (1981b) model calculations.

I would like to thank M. Standish for providing the ephemerides of Jupiter at the times of the observations, and M. J. Klein for comments on the manuscript. This research was supported by NSF Grant No. AST-8900156, NASA Grant No. NAGW-1805, and Calspace Grant No. CS-67-1989.

REFERENCES

Baars, J. W. M., Genzel, R., Pauliny-Toth, I. I. K., and Witzel, A. 1977, A&A, 61, 99
Berge, G. L., and Gulkis, S. 1976, in Jupiter, edited by T. Gehrels (University of Arizona Press, Tucson, Arizona), pp. 621–692
Branson, N. J. B. A. 1968, MNRAS, 139, 155
z Carr, T. D., Desch, M. D., and Alexander, J. K. 1983, in Physics of the Jovian Magnetosphere, edited by A. J. Dessler (Cambridge University Press, Cambridge), pp. 226–284
Clark, B. G. 1980, A&A, 89, 377
de Pater, I. 1980, A&A, 88, 175
de Pater, I. 1981a, A&A, 93, 370
de Pater, I. 1981b, J. Geophys. Res., 86, 3397
de Pater, I. 1981c, J. Geophys. Res., 86, 3423
de Pater, I. 1983, Adv. Space Res., 3, 31
de Pater, I. 1990, ARA&A, 28, 347
de Pater, I., and Dames, H. A. C. 1979, A&A, 72, 148
de Pater, I., and Jaffe, W. J. 1984, ApJS, 54, 405
de Pater, I., and Klein, M. J. 1989, in Proceedings of the International Workshop on Time Variable Phenomena in the Jovian System, Flagstaff, Arizona, August, 1987, pp. 139–150
Högbom, J. A. 1974, A&AS, 15, 417
Klein, M. J. 1976, J. Geophys. Res., 81, 3380
Klein, M. J., Thompson, T. J., and Bolton, S. J. 1989, in Proceedings of the International Workshop on Time Variable Phenomena in the Jovian System, Flagstaff, Arizona, August, 1987, pp. 151–155
Morris, D., Berge, G. L. 1962, ApJ, 136, 276
Neidhöfer, J. 1978, Ph.D. dissertation, University of Bonn, West Germany
Neidhöffer, J., Booth, R. S., Morris, D., Wilson, W., Biraud, F., and Ribes, J.-C. 1977, A&A, 61, 321
Roberts, J. A., and Komesaroff, M. M. 1965, Icarus, 4, 127
Van Allen, J. A. 1976, in Jupiter, edited by T. Gehrels (University of Arizona Press, Tucson, Arizona), pp. 928–960